Resonance fluorescence of a hybrid semiconductor-quantum-dot–metal-nanoparticle system driven by a bichromatic field

Atefeh Mohammadzadeh and MirFaez Miri[*]

Department of Physics, University of Tehran, P.O. Box 14395-547, Tehran, Iran

We study the spectrum and statistical properties of photons scattered from a semiconductor-quantum-dot–metal-nanoparticle system under monochromatic and bichromatic excitations. We rely on the Bloch equation to describe the evolution of the density matrix of the quantum dot. We pay attention to the self-interaction of the quantum dot in the presence of the nanoparticle. Going beyond the dipole approximation, we show that the system exhibits optical responses of different character in different regions of the quantum dot dipole moment versus the nanoparticle radius phase diagram. In the strong transition and bistability regions, upon changing the initial state, a pronounced fluorescence spectrum may become a faint one, and an oscillatory intensity-intensity correlation may become a monotonically increasing one. The amplitudes, frequencies, and phases of the laser fields tailor the number, position, height, and width of the peaks of the fluorescence spectrum. The antibunched light as well as the sub-Poissonian light can be generated. Our results suggest that in view of solid-state-based sources of nonclassical light, a hybrid quantum-dot–nanoparticle system may be superior to an isolated quantum dot.

I. INTRODUCTION

As early as 1969, Mollow predicted the three-peaked fluorescence spectrum of a two-level system resonantly driven by a strong monochromatic laser field [1]. The spectrum consists of a central peak centered at the laser field frequency and two symmetrically placed sidebands shifted from the central peak by the Rabi frequency of the laser field. The sidebands are $1/3$ as high as and $3/2$ as wide as the central peak. The Mollow triplet has been observed in sodium atoms [2] and in single molecules [3]. The fluorescence spectrum of a two-level system driven by a strong bichromatic field [4,5] is substantially different from the Mollow spectrum. Here the number, position, height, and width of peaks all depend on frequencies, phases, and amplitudes of the two laser fields. The resonance fluorescence of two-level-like barium atoms under bichromatic excitation is experimentally measured [6,7].

In view of generation of nonclassical light, resonance fluorescence of two-level systems has gained interest. Photon antibunching in resonance fluorescence [8] from a sodium atom in a beam [9] and a magnesium ion stored in a radio-frequency trap [10] are both observed. Moreover, antibunching between a photon from a sideband and a photon from the central peak, bunching between two photons from opposite sidebands, and antibunching between two photons from a sideband were theoretically predicted and experimentally demonstrated in strontium and barium atoms [11,12]. Recently, the correlations of photons away from the Mollow peaks and at the appropriate frequencies have been hailed as a resource of heralded *N*-photon bundles [13].

With the recent surge in interest in quantum cryptography, quantum computing, quantum sensing, and quantum metrology, many studies have been devoted to *solid-state-based light sources* for nonclassical light generation. Utilizing semiconductor quantum dots (SQDs)—which are artificial atoms to some extent—important progress has been made [14–16]. Realization of a single-photon turnstile device [17], a source of triggered entangled photon pairs [18,19], spin-resolved resonance fluorescence [20], and cascaded single-photon emission from the Mollow triplet sidebands [21] are reported. Bichromatic driving of SQDs has also gained attention: The Autler-Townes splitting and gain without inversion in the Mollow absorption spectrum [22], oscillations at half the difference of the laser frequencies and harmonics thereof in the case of resonant light scattering [23], and the interference-induced spectral line elimination [24] were experimentally demonstrated. These may pave the way towards utilizing SQDs for optical modulators [25], Mollow dressed-state lasers [26,27], and a heralded source of *N*-photon bundles [13].

On the other hand, metallic nanoparticles (MNPs) continue to receive attention due to their optical properties [28]. In view of the development of new photonic devices, hybrid SQD-MNP systems have been thoroughly studied [29–52]. Due to the interaction of excitons and surface plasmons, the optical response of a hybrid SQD-MNP system markedly differs from those of SQD and MNP. For instance, a hybrid SQD-MNP system exhibits bistability [31–33]. Indeed, excitation of the localized surface plasmons of MNP gives rise to an enhanced electric field in the nearby SQD. The dipole moment of the SQD induces multipole moments in the MNP, which leads to an extra electric field in the SQD. This feedback mechanism is the origin of the bistability of the hybrid system.

---
[*]mirfaez_miri@ut.ac.ir

To describe the interaction of the light and the hybrid SQD-MNP system, the simplest model treats the incident field as a classical electromagnetic field, the SQD as a two-level system, and the MNP as a classical spherical particle [31,33–35,38,48–51]. The SQD dipole moment μ and the MNP radius a greatly influence the *absorption* of a system driven by an external field $E_1 \cos(\omega_1 t)$. Within the dipole approximation, the μ versus a phase diagram consists of five regions. The asymmetrical Fano shape of the MNP absorption spectrum [48], exciton-induced transparency (EXIT) in the MNP absorption spectrum, and bistability of the system [49] characterize three regions of the phase diagram. Weak-transition (WT) and strong-transition (ST) regions between the EXIT and the bistability regions are also identified [50]. In the WT and ST regions of the phase diagram, the level population difference versus the driving frequency exhibits asymmetry and a discontinuous jump, respectively. Taking into account multipole polarization in MNP [51], we have shown that the borders between all regions of the absorption phase diagram move substantially [52]. Moreover, EXIT does not occur in the strict sense. Nevertheless, a double-peak region exists where the ratio of the maximum over the minimum of MNP absorption is less than a threshold.

Exploiting the exciton-plasmon interaction to manipulate the resonance fluorescence spectrum of a SQD close to a MNP is the subject of ongoing research [53–60]. It is shown that the Coulomb interaction modifies the position and width of the peaks of the fluorescence spectrum and the statistical properties of the photons. In these studies, only the case of a monochromatic driving field is considered. But driving the system with two fields of different frequencies, amplitudes, and phases may allow one to engineer the fluorescence spectrum and to turn it into a *tuneable* source of N-photon bundles [13]. More importantly, the decisive role of the self-interaction of the SQD in the presence of the MNP has been overlooked in most studies of the fluorescence spectrum and the intensity-intensity correlation function. But in the ST and bistability regions of the phase diagram, multipole effects are considerable. There is another good reason to consider the influence of multipole effects on the fluorescence spectrum of the hybrid system: Quantum light opens new horizons for spectroscopy by employing parameters of the quantum state of light and the photon statistics to detect the matter properties [61]. In the recently introduced "Mollow spectroscopy" technique, one excites the target system with the resonance fluorescence [62].

In this paper, we go *beyond* the dipole approximation to calculate the spectrum and statistical properties of photons scattered from a SQD-MNP system under monochromatic and *bichromatic* excitations. We find that the hybrid system exhibits optical responses of different character in different regions of the μ versus a phase diagram. Indeed, in the ST and bistability regions of the phase diagram, the fluorescence spectrum and the intensity-intensity correlation function may depend on the initial state of the system: Upon changing the initial population inversion, a pronounced spectrum may become a faint one, and an oscillatory intensity-intensity correlation may become a monotonically increasing one. We find that the amplitudes, frequencies, and phases of the laser fields can be invoked to tailor the number, position, height,
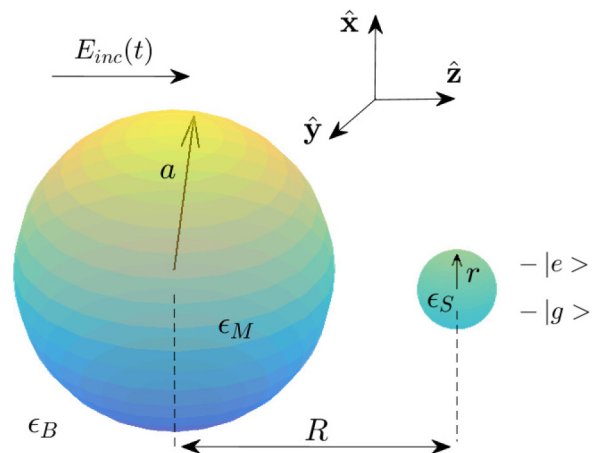

FIG. 1. Schematics of a hybrid system composed of one spherical MNP and one spherical SQD. The system is subject to the incident electric field $E_{\text{inc}}(t)$.

and width of the peaks of the fluorescence spectrum. The antibunched light as well as the sub-Poissonian light can be generated.

II. MODEL

We study a hybrid system composed of one spherical MNP of radius a and one spherical SQD of radius r, separated by a center-to-center distance R (see Fig. 1). We choose the axis of the hybrid system as the $\hat{z}$ axis and assume that the MNP and the SQD are centered at $(0,0,0)$ and $(0, 0, R)$, respectively. The hybrid system is subject to the incident electric field $E_{\text{inc}}(t)$.

We treat the MNP as a classical dielectric sphere with dielectric function ϵ_M, embedded in a medium with dielectric function ϵ_B. We model the SQD as a two-level system with ground state $|g\rangle$ and excited state $|e\rangle$. The Hamiltonian of the SQD is

$$H_{\text{SQD}} = \varepsilon_g |g\rangle\langle g| + \varepsilon_e |e\rangle\langle e| - \mu E_{\text{SQD}}(t)(|g\rangle\langle e| + |e\rangle\langle g|), \quad (1)$$

where $\varepsilon_g = \hbar\omega_g$ is the ground-state energy, $\varepsilon_e = \hbar\omega_e$ is the excited-state energy, $\omega_{eg} = \omega_e - \omega_g$ is the transition frequency, μ is the optical transition dipole moment, and $E_{\text{SQD}}(t)$ is the total electric field felt by the SQD. We rely on the phenomenological Bloch equation [63]

$$\frac{d\rho}{dt} = \frac{i}{\hbar}[\rho, H_{\text{SQD}}] - \Gamma(\rho) \quad (2)$$

to describe the evolution of the density matrix

$$\rho = \begin{pmatrix} \rho_{ee} & \rho_{eg} \\ \rho_{ge} & \rho_{gg} \end{pmatrix}$$

of the SQD. Here the phenomenological decay term $\Gamma(\rho)$ describes the relaxation processes. The density matrix enables us to access various quantities, for instance, the polarization of the SQD, $P_{\text{SQD}} = \mu(\rho_{ge} + \rho_{eg})$.

III. RESONANCE FLUORESCENCE SPECTRUM

We aim to show the impact of exciton-plasmon interaction on the resonance fluorescence spectrum of the hybrid system.

We first recall that the presence of a MNP markedly influences the electric field $E_{SQD}(t)$ inside the SQD.

We assume that the system is subject to the biharmonic electric field

$$E_{inc}(t) = E_1 \cos(\omega_1 t + \phi_1) + E_2 \cos(\omega_2 t + \phi_2). \quad (3)$$

The direction of the incident field $\hat{e}$ is either parallel or perpendicular to the axis of the system $\hat{z}$. The electric field $E_{SQD}(t)$ has three components [51],

$$E_{SQD}(t) = \frac{1}{\epsilon_{effS}}[E_{inc}(t) + E_{M \to S}(t) + E_{S \to S}(t)]. \quad (4)$$

Indeed, the first component $E_{inc}(t)/\epsilon_{effS}$ originates from the incident electric field. Here the factor $\epsilon_{effS} = (\epsilon_S + 2\epsilon_B)/(3\epsilon_B)$ emphasizes the difference of fields outside and inside a SQD of dielectric function ϵ_S. Note that it is assumed that in the vicinity of ω_{eg} both ϵ_S and ϵ_B are real numbers and exhibit no strong frequency dependence. The electric field

$$E_{M \to S}(t) = \frac{s_{pol}\alpha_1^*}{2R^3}(E_1 e^{i\omega_1 t + i\phi_1} + E_2 e^{i\omega_2 t + i\phi_2})$$
$$+ \frac{s_{pol}\alpha_1}{2R^3}(E_1 e^{-i\omega_1 t - i\phi_1} + E_2 e^{-i\omega_2 t - i\phi_2}), \quad (5)$$

where $\alpha_1 = a^3(\epsilon_M - \epsilon_B)/(\epsilon_M + 2\epsilon_B)$ and $s_{pol} = 2$ and -1 for $\hat{e} \parallel \hat{z}$ and $\hat{e} \perp \hat{z}$, respectively. Incidentally, the incident field induces an electric dipole moment in the MNP. This electric dipole moment leads to the second component of the electric field inside the SQD. The electric field

$$E_{S \to S}(t) = \frac{1}{\epsilon_B}\left(\sum_{l=1}^{\infty}\frac{\mu\alpha_l^* s_l}{R^{2l+4}}\rho_{ge} + \sum_{l=1}^{\infty}\frac{\mu\alpha_l s_l}{R^{2l+4}}\rho_{eg}\right), \quad (6)$$

where $\alpha_l = la^{2l+1}(\epsilon_M - \epsilon_B)/[l\epsilon_M + (l+1)\epsilon_B]$ and the coefficient $s_l = (l+1)^2$ and $l(l+1)/2$ for $\hat{e} \parallel \hat{z}$ and $\hat{e} \perp \hat{z}$, respectively. Note that the dipole P_{SQD} induces oscillating multipole moments in the MNP. These multipole moments lead to the third component of the electric field inside the SQD, which portrays the self-interaction of the SQD in the presence of the MNP. The decisive influence of the electric field $E_{S \to S}(t)$ on the fluorescence spectrum has been overlooked in most previous studies.

The electric field $E_{SQD}(t)$ can be written as

$$E_{SQD}(t) = \frac{\hbar}{\mu}[\Omega_1 e^{-i\omega_1 t - i\phi_1} + \Omega_2 e^{-i\omega_2 t - i\phi_2} + G\rho_{eg}$$
$$+ \Omega_1^* e^{i\omega_1 t + i\phi_1} + \Omega_2^* e^{i\omega_2 t + i\phi_2} + G^*\rho_{ge}], \quad (7)$$

where

$$\Omega_1 = \frac{E_1\mu}{2\hbar\epsilon_{effS}}\left(1 + \frac{s_{pol}\alpha_1}{R^3}\right),$$

$$\Omega_2 = \frac{E_2\mu}{2\hbar\epsilon_{effS}}\left(1 + \frac{s_{pol}\alpha_1}{R^3}\right),$$

$$G = \frac{\mu^2}{\hbar\epsilon_B\epsilon_{effS}}\sum_{l=1}^{\infty}\frac{s_l\alpha_l}{R^{2l+4}}. \quad (8)$$

Within the rotating wave approximation [52]

$$H_{SQD} \approx \begin{pmatrix} \varepsilon_e & -\varepsilon_o(t) \\ -\varepsilon_o^*(t) & \varepsilon_g \end{pmatrix}, \quad (9)$$

where $\varepsilon_o(t) = \hbar(\Omega_1 e^{-i\omega_1 t - i\phi_1} + \Omega_2 e^{-i\omega_2 t - i\phi_2} + G\rho_{eg})$.

Now we recast the Bloch equation (2). We introduce $\phi_p = (\phi_2 + \phi_1)/2$, $\phi_n = (\phi_2 - \phi_1)/2$, $\omega_p = (\omega_2 + \omega_1)/2$, $\omega_n = (\omega_2 - \omega_1)/2$, $U = \text{diag}(e^{-i(\omega_p t + \phi_p)/2}, e^{i(\omega_p t + \phi_p)/2})$, $\tilde{\rho} = U^{-1}\rho U$, $\tilde{H}_{SQD} = U^{-1}H_{SQD}U$, and $\tilde{H}_U = i\hbar U^{-1}\dot{U}$. The Bloch equation then reads

$$\frac{d\tilde{\rho}}{dt} = \frac{i}{\hbar}[\tilde{\rho}, \tilde{H}_{SQD} - \tilde{H}_U] - \Gamma(\tilde{\rho}), \quad (10)$$

where

$$\tilde{\rho}_{eg} = \rho_{eg}e^{i\omega_p t + i\phi_p},$$
$$\tilde{\rho}_{ge} = \rho_{ge}e^{-i\omega_p t - i\phi_p},$$
$$\tilde{\omega}_o(t) = \Omega_1 e^{i\omega_n t + i\phi_n} + \Omega_2 e^{-i\omega_n t - i\phi_n} + G\tilde{\rho}_{eg},$$
$$\tilde{H}_{SQD} - \tilde{H}_U = \hbar\begin{pmatrix} \omega_e - \omega_p/2 & -\tilde{\omega}_o(t) \\ -\tilde{\omega}_o^*(t) & \omega_g + \omega_p/2 \end{pmatrix}. \quad (11)$$

Note that the $e^{\pm i\omega_n t}$ terms of $\tilde{H}_{SQD} - \tilde{H}_U$ oscillate much slower than the $e^{\pm i\omega_1 t}$ and $e^{\pm i\omega_2 t}$ terms of H_{SQD}. This shows that it is advantageous to apply the unitary transformation to the density matrix. We adopt

$$\Gamma(\tilde{\rho}) = \begin{pmatrix} \frac{\rho_{ee}}{\tau_0} & \frac{\tilde{\rho}_{eg}}{T_0} \\ \frac{\tilde{\rho}_{ge}}{T_0} & -\frac{1-\rho_{gg}}{\tau_0} \end{pmatrix} \quad (12)$$

for the phenomenological description of the relaxation processes. Indeed, τ_0 and T_0 are the relaxation constants of the population and the dipole dephasing, respectively. For an arbitrary operator A, we denote $\langle A \rangle = \text{Tr}(\tilde{\rho}A)$ and $\delta A = A - \langle A \rangle$. Now using operators $S_+ = |e\rangle\langle g|$, $S_- = |g\rangle\langle e|$, and $S_z = |e\rangle\langle e| - |g\rangle\langle g|$, the Bloch equation can be recast as

$$\begin{pmatrix} \langle \dot{S}_-(t) \rangle \\ \langle \dot{S}_+(t) \rangle \\ \langle \dot{S}_z(t) \rangle \end{pmatrix} = M(t)\begin{pmatrix} \langle S_-(t) \rangle \\ \langle S_+(t) \rangle \\ \langle S_z(t) \rangle \end{pmatrix} - \begin{pmatrix} 0 \\ 0 \\ \frac{1}{\tau_0} \end{pmatrix}, \quad (13)$$

where

$$M(t) = \begin{pmatrix} -i\Delta - \frac{1}{T_0} & 0 & -i\tilde{\omega}_o(t) \\ 0 & i\Delta - \frac{1}{T_0} & i\tilde{\omega}_o^*(t) \\ -2i\tilde{\omega}_o^*(t) & 2i\tilde{\omega}_o(t) & -\frac{1}{\tau_0} \end{pmatrix}, \quad (14)$$

and the detuning is $\Delta = \omega_{eg} - \omega_p$. In two limits, a monochromatic driving field ($E_2 \to 0$ and $\omega_2 \to \omega_1$) and a large SQD-MNP separation ($R \to \infty$), the Bloch equation (13) is consistent with that of previous studies [4,50,52].

To access the *far* field emitted by the hybrid system, it is sufficient to consider the electric dipole operator in the rotating frame

$$P^{Hyb}(t) = \left[\frac{\alpha_1^*}{2}(E_1 e^{-i\omega_n t - i\phi_n} + E_2 e^{i\omega_n t + i\phi_n})\right.$$
$$+ \frac{\alpha_1}{2}(E_1 e^{i\omega_n t + i\phi_n} + E_2 e^{-i\omega_n t - i\phi_n})\right]$$
$$+ [\mu S_+(t) + \mu S_-(t)]$$
$$+ \left[\frac{\mu s_{pol}\alpha_1^*}{R^3}S_+(t) + \frac{\mu s_{pol}\alpha_1}{R^3}S_-(t)\right]. \quad (15)$$

Note that the dipole moments of the MNP and the SQD are parallel. The first component of P^{Hyb} represents the dipole moment induced in the MNP by the biharmonic incident

field. The second component portrays the dipole moment of the SQD. The third component, which vanishes in the limit $R \rightarrow \infty$, represents the dipole moment induced in the MNP by the SQD. The spectrum of the light scattered incoherently by the hybrid system is [1]

$$
\mathcal{S}_{\text{Hyb}}(\omega) = \text{Re}\left(\int_0^T \frac{2dt_0}{T} \int_0^\infty \frac{d\tau}{\mu^2 \tau_0} \langle \delta P_+^{\text{Hyb}}(t_0) \right. \\
\left. \times \, \delta P_-^{\text{Hyb}}(t_0 + \tau) \rangle e^{i(\omega - \omega_p)\tau} \right),
$$

(16)

where $P_+^{\text{Hyb}}(t)$ [$P_-^{\text{Hyb}}(t)$] denotes the positive (negative) frequency part of the operator $P^{\text{Hyb}}(t)$. Of course, in the limit $R \rightarrow \infty$, the above spectrum tends towards $\mathcal{S}_{\text{Iso}}(\omega)$ of an isolated SQD. Here the factor $\mu^2 \tau_0$ is used to make $\mathcal{S}_{\text{Hyb}}(\omega)$ dimensionless.

Indeed, $\langle \delta P_+^{\text{Hyb}}(t_0) \delta P_-^{\text{Hyb}}(t_0 + \tau) \rangle = \mu^2 \, |1 + s_{\text{pol}} \alpha_1 / R^3|^2$ $\langle \delta S_+(t_0) \delta S_-(t_0 + \tau) \rangle$. This invites us to calculate the two-time correlation functions

$$
C(t_0, \tau) = \begin{pmatrix} \langle \delta S_+(t_0) \delta S_-(t_0 + \tau) \rangle \\ \langle \delta S_+(t_0) \delta S_+(t_0 + \tau) \rangle \\ \langle \delta S_+(t_0) \delta S_z(t_0 + \tau) \rangle \end{pmatrix}.
$$

(17)

According to the quantum regression theorem [63],

$$
\frac{d}{d\tau} C(t_0, \tau) = M(t_0 + \tau) C(t_0, \tau).
$$

(18)

To solve this equation, the initial value $C(t_0, 0)$ must be specified. Here the identities

$$
\langle \delta S_+(t_0) \delta S_-(t_0) \rangle = \frac{1}{2} + \frac{1}{2} \langle S_z(t_0) \rangle - |\langle S_+(t_0) \rangle|^2,
$$

$$
\langle \delta S_+(t_0) \delta S_+(t_0) \rangle = -\langle S_+(t_0) \rangle^2,
$$

$$
\langle \delta S_+(t_0) \delta S_z(t_0) \rangle = -\langle S_+(t_0) \rangle - \langle S_+(t_0) \rangle \langle S_z(t_0) \rangle
$$

(19)

are of great use.

IV. ANTIBUNCHING OF THE FLUORESCENT PHOTONS

A two-level system cannot emit two photons at once because a finite time is required to cycle between the ground and excited states. In other words, the fluorescent light emitted by a two-level system exhibits photon antibunching [8]. The radiation from a classic dipole is second order coherent or Poissonian. Here we consider a hybrid SQD-MNP system and investigate whether the exciton-plasmon interaction exerts influence on the photon statistics.

The electric dipole operator $P^{\text{Hyb}}(t)$ determines the far-zone electric field emitted by the hybrid system. The statistical properties of the fluorescent photons can be determined through the second-order normalized correlation function [23,64]

$$
G^{(2)}(\tau) = \frac{\overline{\langle P_+^{\text{Hyb}}(t_0) P_+^{\text{Hyb}}(t_0 + \tau) P_-^{\text{Hyb}}(t_0 + \tau) P_-^{\text{Hyb}}(t_0) \rangle}}{\overline{\langle P_+^{\text{Hyb}}(t_0) P_-^{\text{Hyb}}(t_0) \rangle} \, \overline{\langle P_+^{\text{Hyb}}(t_0 + \tau) P_-^{\text{Hyb}}(t_0 + \tau) \rangle}}.
$$

(20)

Here the overline denotes averaging with respect to the time t_0. The most complicated term in the numerator of $G^{(2)}(\tau)$ is proportional to $\langle S_+(t_0) S_+(t_0 + \tau) S_-(t_0 + \tau) S_-(t_0) \rangle = \frac{1}{4}[1 +$
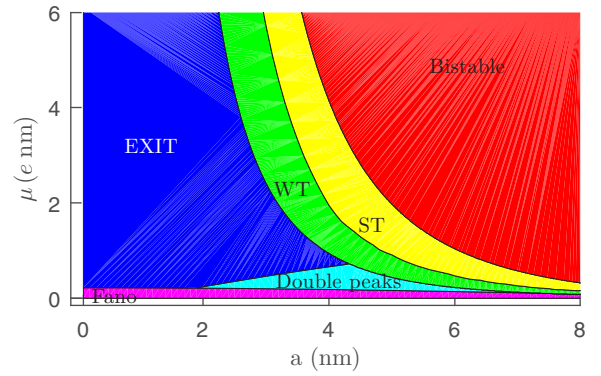

FIG. 2. μ versus a phase diagram in the strong-field limit for $\boldsymbol{E}_{\text{inc}} = E_1 \cos(\omega_1 t) \hat{z}$, $R = 13$ nm, and $I_1 = 10^3$ W/cm^2. The acronyms stand for exciton-induced transparency (EXIT), weak transition (WT), and strong transition (ST). See also Fig. 2 in Ref. [52].

$\langle S_z(t_0) \rangle] + \frac{1}{2} \langle S_+(t_0) S_z(t_0 + \tau) S_-(t_0) \rangle$. This invites us to study the correlation functions

$$
C_s(t_0, \tau) = \begin{pmatrix} \langle S_+(t_0) S_-(t_0 + \tau) S_-(t_0) \rangle \\ \langle S_+(t_0) S_+(t_0 + \tau) S_-(t_0) \rangle \\ \langle S_+(t_0) S_z(t_0 + \tau) S_-(t_0) \rangle \end{pmatrix}.
$$

(21)

According to the quantum regression theorem,

$$
\frac{d}{d\tau} C_s(t_0, \tau) = M(t_0 + \tau) C_s(t_0, \tau) - \begin{pmatrix} 0 \\ 0 \\ \frac{1 + \langle S_z(t_0) \rangle}{2\tau_0} \end{pmatrix}.
$$

(22)

The numerical solution of this equation with the initial value $C_s(t_0, 0) = (0, 0, -\frac{1 + \langle S_z(t_0) \rangle}{2})^{\text{T}}$ allows us to calculate $G^{(2)}(\tau)$.

V. RESULTS

To gain better insight into the optical response of the hybrid system, one can view the SQD as a damped harmonic oscillator whose response to a driving field changes from in phase to out of phase near the natural frequency [50]. Indeed, the *interference* of the incident field E_{inc}, MNP-induced field $E_{\text{M} \rightarrow \text{S}}$, and the self-interaction mediated by the MNP $E_{\text{S} \rightarrow \text{S}}$ drives the SQD [see Eq. (4)]. The driving field depends on *both* the SQD dipole moment and the MNP radius [see Eq. (7)]. The constructive or destructive interference of E_{inc}, $E_{\text{M} \rightarrow \text{S}}$, and $E_{\text{S} \rightarrow \text{S}}$ also determines the total dipole moment of the hybrid system [see Eq. (15)]; thus, the system exhibits fluorescence spectra of different character in different regions of the phase diagram. This will be demonstrated by the following examples.

Following Refs. [48,50,52], we consider a system with $\omega_{eg} = 2.5$ eV, $\tau_0 = 0.8$ ns, $T_0 = 0.3$ ns, $\epsilon_S = 6$, $\epsilon_B = 1$, and $R = 13$ nm. Near the transition frequency, $\epsilon_M = -2.28 + 3.81i$ serves as the bulk dielectric constant of gold [65]. We focus on the case $\hat{e} = \hat{z}$.

We exemplify the fluorescence spectrum for five points (a, μ) of the phase diagram: $F_{\text{pd}} = (7, 0.1)$ in the Fano region, $E_{\text{pd}} = (3, 2)$ in the EXIT region, $W_{\text{pd}} = (6, 0.5)$ in the WT region, $S_{\text{pd}} = (6, 1)$ in the ST region, and $B_{\text{pd}} = (6, 2)$ in the bistability regions of the phase diagram (see Fig. 2). Here the radius a is in nanometers, and the dipole moment μ is
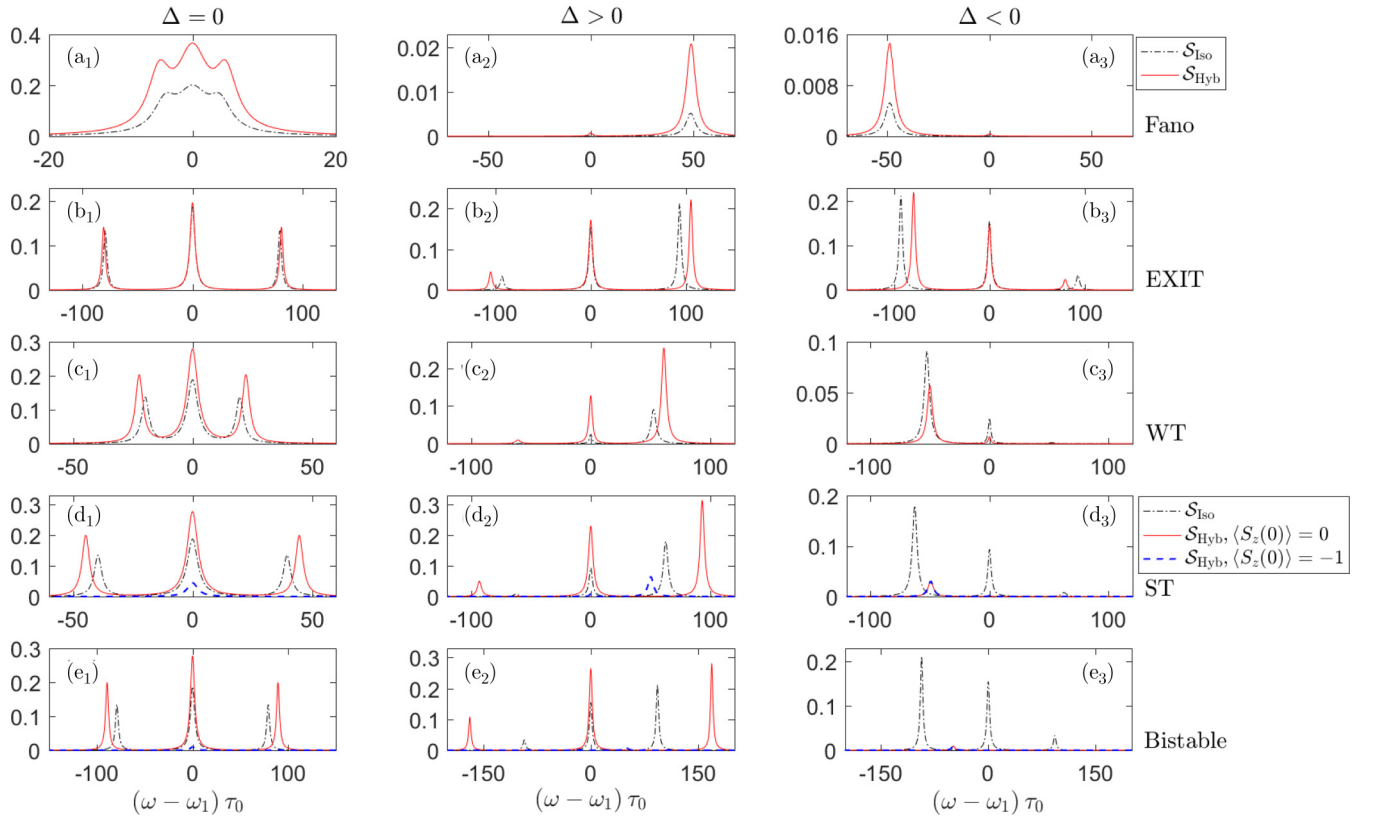
FIG. 3. $\mathcal{S}_{\mathrm{Iso}}$ and $\mathcal{S}_{\mathrm{Hyb}}$ versus $\omega - \omega_1$ at the points (a) F_{pd}, (b) E_{pd}, (c) W_{pd}, (d) S_{pd}, and (e) B_{pd}. $\Delta\tau_0$ is 0, 48.62, and -48.62 in the left, middle, and right panels, respectively. Here $E_{\mathrm{inc}}(t) = E_1 \cos(\omega_1 t)$ and $I_1 = 10^3$ W/cm^2.

in e nanometers. To provide information on the position and height of peaks of the spectrum, we let tuples of the form $(p_1, \ldots, p_N)$ refer to N successive peaks.

A. Fluorescence spectrum: Monochromatic driving

We first consider a monochromatic driving field $E_{\mathrm{inc}}(t) = E_1 \cos(\omega_1 t)$ whose intensity is $I_1 = 10^3$ W/cm^2. Indeed, for such high incident intensities, the interference of comparable induced and incident fields leads to interesting effects. Figure 3 shows that $\mathcal{S}_{\mathrm{Hyb}}(\omega)$ and $\mathcal{S}_{\mathrm{Iso}}(\omega)$ are distinct. At point F_{pd} of the phase diagram, both $\mathcal{S}_{\mathrm{Iso}}(\omega)$ and $\mathcal{S}_{\mathrm{Hyb}}(\omega)$ have three peaks when the detuning is zero. However, the peaks of $\mathcal{S}_{\mathrm{Hyb}}(\omega)$ are stronger and farther apart than those of $\mathcal{S}_{\mathrm{Iso}}(\omega)$. In detail, three peaks of $\mathcal{S}_{\mathrm{Iso}}(\omega)$ at $(\omega - \omega_1)\tau_0 = (-3.5, 0, 3.5)$ experience an increase by a factor of $(1.74, 1.81, 1.70)$ and shift to $(\omega - \omega_1)\tau_0 = (-4.5, 0, 4.5)$ as the SQD and the MNP come close. Moreover, for either positive or negative detunings, the single pronounced peak of $\mathcal{S}_{\mathrm{Hyb}}(\omega)$ is stronger than that of $\mathcal{S}_{\mathrm{Iso}}(\omega)$ [see Figs. 3(a1)–3(a3)]. At point E_{pd}, the peaks of $\mathcal{S}_{\mathrm{Hyb}}(\omega)$ and $\mathcal{S}_{\mathrm{Iso}}(\omega)$ have almost the same height. For positive (negative) detuning, the sidebands shift outwards (inwards) the central peak as the hybrid system forms [see Figs. 3(b1)–3(b3)]. In the case of point W_{pd}, the peaks of $\mathcal{S}_{\mathrm{Hyb}}(\omega)$ are stronger (weaker) than those of $\mathcal{S}_{\mathrm{Iso}}(\omega)$ when the detuning is zero or positive (negative). In detail, $\mathcal{S}_{\mathrm{Iso}}(\omega)$ has three peaks at $(\omega - \omega_1)\tau_0 = (-52, 0, 52)$ when $\Delta\tau_0 = 48.62$. These peaks experience an increase by a factor of $(9.9, 5.1, 2.8)$ and a widening by a factor of $(0.9, 1.3, 0.9)$ and, finally, shift

to $(\omega - \omega_1)\tau_0 = (-61, 0, 61)$ as the SQD and the MNP come close [see Figs. 3(c1)–3(c3)].

Figure 3 shows that in the ST and bistability regions of the phase diagram, $\mathcal{S}_{\mathrm{Hyb}}(\omega)$ is far more interesting. First, $\mathcal{S}_{\mathrm{Hyb}}(\omega)$ depends on the *initial state* of the system. Second, $\mathcal{S}_{\mathrm{Hyb}}(\omega)$ and $\mathcal{S}_{\mathrm{Iso}}(\omega)$ possess markedly distinct peaks. At point S_{pd}, $\mathcal{S}_{\mathrm{Iso}}(\omega)$ has three peaks at $(\omega - \omega_1)\tau_0 = (-39.5, 0, 39.5)$ when $\Delta = 0$. For an initial state $\langle S_z(0)\rangle = 0$, the corresponding peaks of $\mathcal{S}_{\mathrm{Hyb}}(\omega)$ experience an increase by a factor of $(1.47, 1.48, 1.47)$ and shift to $(\omega - \omega_1)\tau_0 = (-44.5, 0, 44.5)$. But for an initial state $\langle S_z(0)\rangle = -1$, $\mathcal{S}_{\mathrm{Hyb}}(\omega)$ has only *one* central peak at $\omega - \omega_1 = 0$ whose height has been reduced by a factor of 0.24. For positive detuning $\Delta\tau_0 = 48.62$, the strongest peaks for initial states $\langle S_z(0)\rangle = 0$ and $\langle S_z(0)\rangle = -1$ differ by a factor of 4.8. For negative detuning $\Delta\tau_0 = -48.62$, $\mathcal{S}_{\mathrm{Hyb}}(\omega)$ is not considerable except near $(\omega - \omega_1)\tau_0 = -49$ [see Figs. 3(d1)–3(d3)]. As another example, consider point B_{pd} in the bistability region. For zero and positive detunings, $\mathcal{S}_{\mathrm{Hyb}}(\omega)$ pertaining to initial states $\langle S_z(0)\rangle = 0$ and $\langle S_z(0)\rangle = -1$ are quite distinct. The case of negative detuning deserves special attention since here the fluorescence spectrum becomes vanishingly small as the MNP approaches the SQD [see Figs. 3(e1)–3(e3)].

B. Fluorescence spectrum: Bichromatic driving

Incidentally, the resonance fluorescence spectrum of an *isolated* SQD driven by a bichromatic field differs in many
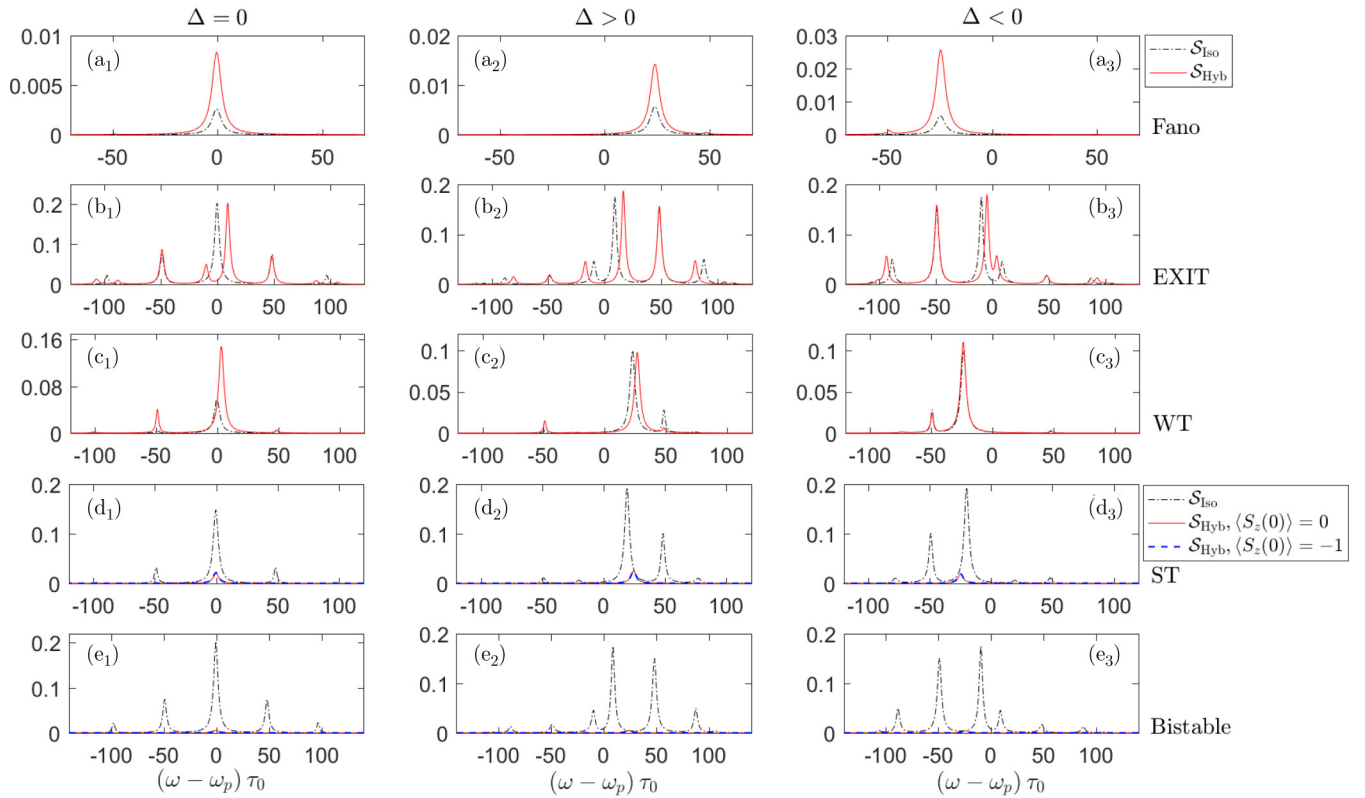
FIG. 4. $\mathcal{S}_{\mathrm{Iso}}$ and $\mathcal{S}_{\mathrm{Hyb}}$ versus $\omega - \omega_p$ at the points (a) F_{pd}, (b) E_{pd}, (c) W_{pd}, (d) S_{pd}, and (e) B_{pd}. $\Delta\tau_0$ is 0, 24.31, and -24.31 in the left, middle, and right panels, respectively. Here $E_{\mathrm{inc}}(t) = E_1 \cos(\omega_1 t) + E_2 \cos(\omega_2 t)$, $\omega_n \tau_0 = 48.62$, and $I_1 = I_2 = 250 \text{ W/cm}^2$.

respects from the three-peaked spectrum for a monochromatic field. As an example we consider a bichromatic field with $\omega_n \tau_0 = 48.62$, $\phi_1 = \phi_2 = 0$, and $I_1 = I_2 = 250 \text{ W/cm}^2$. Here $\Omega_1 = \Omega_2$. Figure 4 shows $\mathcal{S}_{\mathrm{Iso}}$ as a function of $\omega - \omega_p$ for various a, μ, and $\Delta\tau_0$. Note that at points E_{pd} and B_{pd}, $\mathcal{S}_{\mathrm{Iso}}(\omega)$ exhibits *five* peaks when $\Delta = 0$ [see Figs. 4(b1) and 4(e1)]. At point W_{pd}, the spectrum has three peaks when $\Delta = 0$, but the relative heights of these peaks are *not* 1 : 3 : 1 [see Fig. 4(c1)]. It is convenient to name the central peak of the resonance fluorescence spectrum as the zeroth peak and then identify a sideband to the right or left of the central peak as an odd or even sideband. As the detuning Δ becomes nonzero, not only the central peak but also *even* sidebands split. For example, at point E_{pd} and for $\Delta\tau_0 = 24.31$, the central peak at $(\omega - \omega_p)\tau_0 = 0$ splits into two peaks at $(\omega - \omega_p)\tau_0 = -9$ and 9, which are weaker than the original peak by factors of 0.23 and 0.86, respectively. Similar second sidebands at $(\omega - \omega_p)\tau_0 = \pm 97$ split into dissimilar sidebands at $(\omega - \omega_p)\tau_0 = (-106, -88, 88, 106)$ whose heights are a factor of $(0.10, 0.58, 2.21, 0.20)$ different from the original one [see Fig. 4(b2)].

Now we consider the fluorescence spectrum of a hybrid system driven by the same bichromatic field. Indeed, $\mathcal{S}_{\mathrm{Hyb}}(\omega)$ and $\mathcal{S}_{\mathrm{Iso}}(\omega)$ pertaining to various regions of the phase diagram are distinguishable. At point F_{pd} of the phase diagram, the overall shapes of $\mathcal{S}_{\mathrm{Hyb}}(\omega)$ and $\mathcal{S}_{\mathrm{Iso}}(\omega)$ are almost the same. For all detunings, the main peak of $\mathcal{S}_{\mathrm{Hyb}}(\omega)$ is stronger than that of $\mathcal{S}_{\mathrm{Iso}}(\omega)$ [see Figs. 4(a1)–4(a3)]. At point E_{pd}, $\mathcal{S}_{\mathrm{Hyb}}(\omega)$ does not exhibit a peak at $\omega - \omega_p = 0$ when $\Delta = 0$. Furthermore, the spectrum lacks *mirror symmetry* around a certain

central peak. A closer inspection reveals that, indeed, the central peak and *even* but not odd sidebands of $\mathcal{S}_{\mathrm{Iso}}(\omega)$ were split as the MNP approached the SQD [see Figs. 4(b1)–4(b3)]. At point W_{pd}, $\mathcal{S}_{\mathrm{Hyb}}(\omega)$ exhibits four peaks, although the main peak is not at $\omega - \omega_p = 0$ when $\Delta = 0$. The peaks of $\mathcal{S}_{\mathrm{Hyb}}(\omega)$ are stronger than that of $\mathcal{S}_{\mathrm{Iso}}(\omega)$ when the detuning is zero. In the case of point S_{pd}, $\mathcal{S}_{\mathrm{Hyb}}(\omega)$ exhibits only *one* peak whether $\Delta = 0$ or not. This peak is much weaker than the main peak of $\mathcal{S}_{\mathrm{Iso}}(\omega)$ [see Figs. 4(d1)–4(d3)]. In the case of point B_{pd}, $\mathcal{S}_{\mathrm{Hyb}}(\omega)$ is negligible in comparison to $\mathcal{S}_{\mathrm{Iso}}(\omega)$ [see Figs. 4(e1)–4(e3)]. For these intensities $I_1 = I_2 = 250 \text{ W/cm}^2$, $\mathcal{S}_{\mathrm{Hyb}}(\omega)$ does not depend on the initial state of the system.

For high intensities, $\mathcal{S}_{\mathrm{Hyb}}(\omega)$ may show a dependence on the initial state. This is exemplified in Fig. 5 for $I_1 = I_2 = 1000 \text{ W/cm}^2$. First, note that at point B_{pd} of the phase diagram, $\mathcal{S}_{\mathrm{Iso}}(\omega)$ itself shows *13* peaks in the window $-300 < (\omega - \omega_p)\tau_0 < 300$ when $\Delta = 0$. Among the peaks, the zeroth peak at $\omega - \omega_p = 0$ and the second peaks at $(\omega - \omega_p)\tau_0 = \pm 97$ are noticeable. However, for an initial state $\langle S_z(0)\rangle = 0$, the corresponding $\mathcal{S}_{\mathrm{Hyb}}(\omega)$ shows no peaks therein. Indeed, *odd* sidebands of $\mathcal{S}_{\mathrm{Iso}}(\omega)$ were split as the MNP approached the SQD. But for an initial state $\langle S_z(0)\rangle = -1$, $\mathcal{S}_{\mathrm{Hyb}}(\omega)$ possess a weak peak at $\omega - \omega_p = 0$. Remarkably, for positive (negative) detuning, $\mathcal{S}_{\mathrm{Hyb}}(\omega)$ shows strong (neutral) dependence on the initial state.

To further engineer the fluorescence spectrum of the system, the ratio of the Rabi frequencies $\chi = \Omega_2/\Omega_1 = \sqrt{I_2/I_1}$ and the phase difference $\phi_n = (\phi_2 - \phi_1)/2$ are of use. This point is vividly demonstrated in Fig. 6.
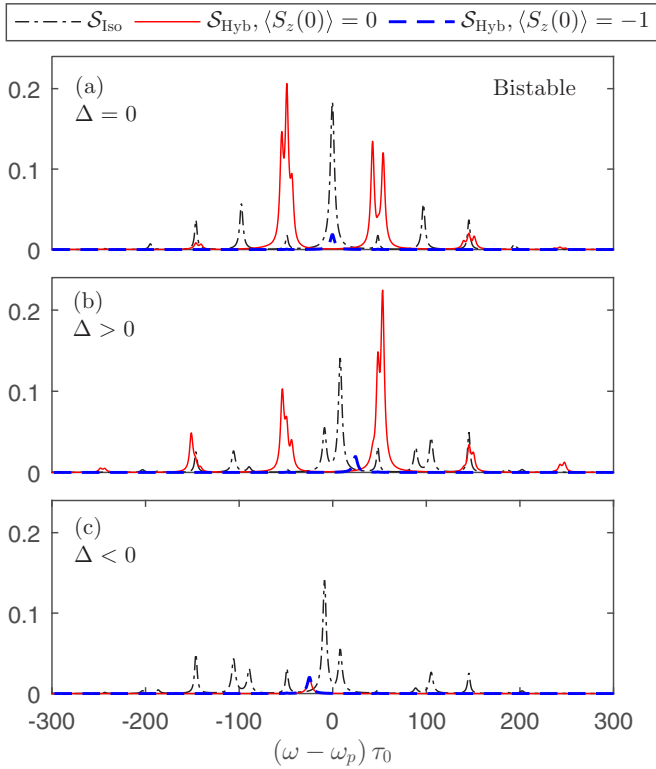
FIG. 5. $\mathcal{S}_{\text{Iso}}$ and $\mathcal{S}_{\text{Hyb}}$ versus $\omega - \omega_p$ at the point B_{pd} for (a) $\Delta = 0$, (b) $\Delta\tau_0 = 24.31$, and (c) $\Delta\tau_0 = -24.31$. Here $\phi_1 = \phi_2 = 0$, $\omega_n\tau_0 = 48.62$, and $I_1 = I_2 = 1000$ W/cm^2.

C. Photon antibunching: Monochromatic driving

Figure 7 depicts $G^{(2)}_{\text{Iso}}(\tau)$ of an isolated SQD and $G^{(2)}_{\text{Hyb}}(\tau)$ of a hybrid SQD-MNP system as a function of the time delay τ when $E_{\text{inc}}(t) = E_1 \cos(\omega_1 t)$ and $\Delta = 0$. In the Fano region of the phase diagram, the behavior of the correlation function is exceptional: $G^{(2)}_{\text{Hyb}}(0) \neq 0$ at point F_{pd}; that is, the fluorescent light does *not* exhibit photon antibunching. Here in determining the antibunching character, the first component of $P^{\text{Hyb}}(t)$ prevails over its second and third components [see Eq. (15)]. At points F_{pd}, E_{pd}, and W_{pd}, $G^{(2)}_{\text{Iso}}(\tau)$ and $G^{(2)}_{\text{Hyb}}(\tau)$ show an oscillatory dependence on τ. The amplitude of these oscillations decreases as τ increases, and finally, both $G^{(2)}_{\text{Iso}}(\tau)$ and $G^{(2)}_{\text{Hyb}}(\tau)$ approach unity as $\tau \to \infty$. The differences of $G^{(2)}_{\text{Iso}}(\tau)$ and $G^{(2)}_{\text{Hyb}}(\tau)$ are transparent at points F_{pd} and W_{pd} of the phase diagram.

Figure 7 shows that in the ST and bistability regions of the phase diagram, the correlation function is far more interesting: $G^{(2)}_{\text{Hyb}}(\tau)$ depends on the *initial state* of the system. Here for the initial state $\langle S_z(0)\rangle = -1$, $G^{(2)}_{\text{Hyb}}(\tau)$ increases monotonically from 0 to 1 as τ increases: $G^{(2)}_{\text{Hyb}}(\tau) < 1$; thus, the light is sub-Poissonian. However, for the initial state $\langle S_z(0)\rangle = 0$, $G^{(2)}_{\text{Hyb}}(\tau)$ mimics $G^{(2)}_{\text{Iso}}(\tau)$ and shows an oscillatory dependence on τ.

D. Photon antibunching: Bichromatic driving

Figure 8 demonstrates $G^{(2)}_{\text{Iso}}(\tau)$ and $G^{(2)}_{\text{Hyb}}(\tau)$ versus τ when $E_{\text{inc}}(t) = E_1 \cos(\omega_1 t) + E_2 \cos(\omega_2 t)$, $\omega_n\tau_0 = 48.62$, $\Delta = 0$,
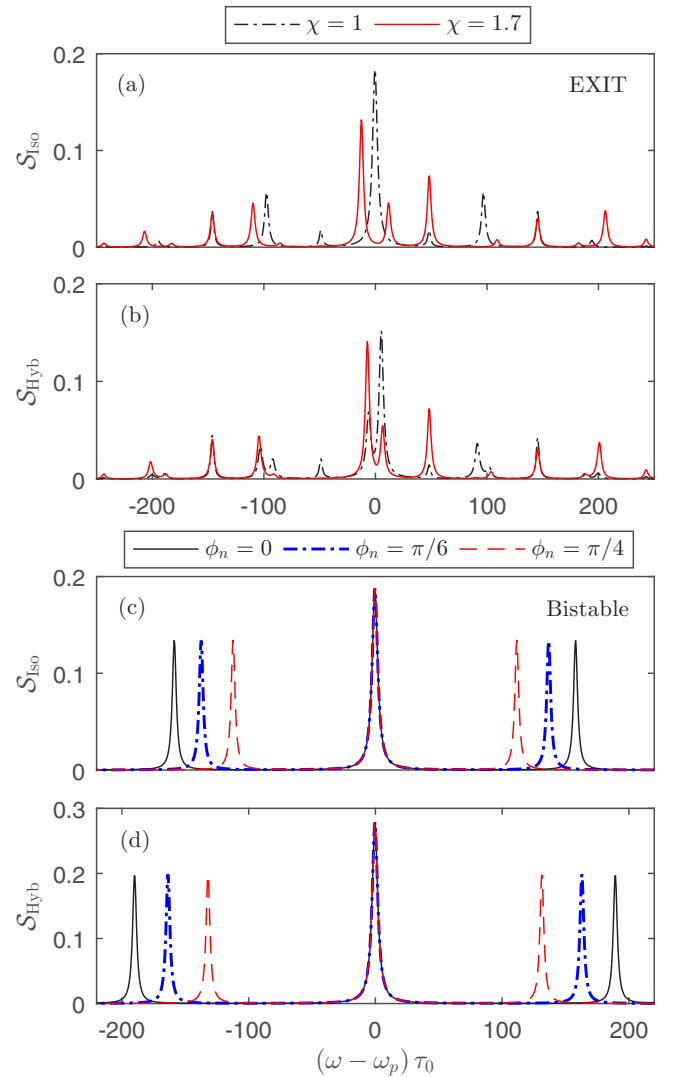

FIG. 6. (a) $\mathcal{S}_{\text{Iso}}$ and (b) $\mathcal{S}_{\text{Hyb}}$ versus $\omega - \omega_p$ at the point E_{pd} for various χ. Here $\phi_1 = \phi_2 = 0$, and $\omega_n\tau_0 = 48.62$. (c) $\mathcal{S}_{\text{Iso}}$ and (d) $\mathcal{S}_{\text{Hyb}}$ versus $\omega - \omega_p$ at the point B_{pd} for various ϕ_n. Here $\omega_n = 0$, $\chi = 1$, $\phi_1 = 0$, and $\langle S_z(0)\rangle = 0$. In all plots $\Delta = 0$ and $I_1 = 1000$ W/cm^2.

and $I_1 = I_2 = 250$ W/cm^2. $G^{(2)}_{\text{Iso}}(\tau)$ and $G^{(2)}_{\text{Hyb}}(\tau)$ are distinct, although both show an oscillatory dependence on τ. At point F_{pd} of the phase diagram, $G^{(2)}_{\text{Iso}}(0) = 0$, but $G^{(2)}_{\text{Hyb}}(0) \neq 0$. Indeed, here $G^{(2)}_{\text{Iso}}(\tau)$ is always less than 1, but $G^{(2)}_{\text{Hyb}}(\tau)$ may exceed 1. At points S_{pd} and B_{pd}, the opposite happens: $G^{(2)}_{\text{Iso}}(\tau)$ may exceed 1, but $G^{(2)}_{\text{Hyb}}(\tau)$ is always less than 1. In other words, the sub-Poissonian nature of light changes as the MNP approaches the SQD. Moreover, at these low intensities, $G^{(2)}_{\text{Hyb}}(\tau)$ does not depend on the initial state of the system. For high intensities, $G^{(2)}_{\text{Hyb}}(\tau)$ may show dependence on the initial state.

VI. CONCLUSION

A few remarks are in order.

(i) The *interference* of E_{inc}, $E_{\text{M}\to\text{S}}$, and $E_{\text{S}\to\text{S}}$ determines the driving field E_{SQD}. The multipole effects change not only

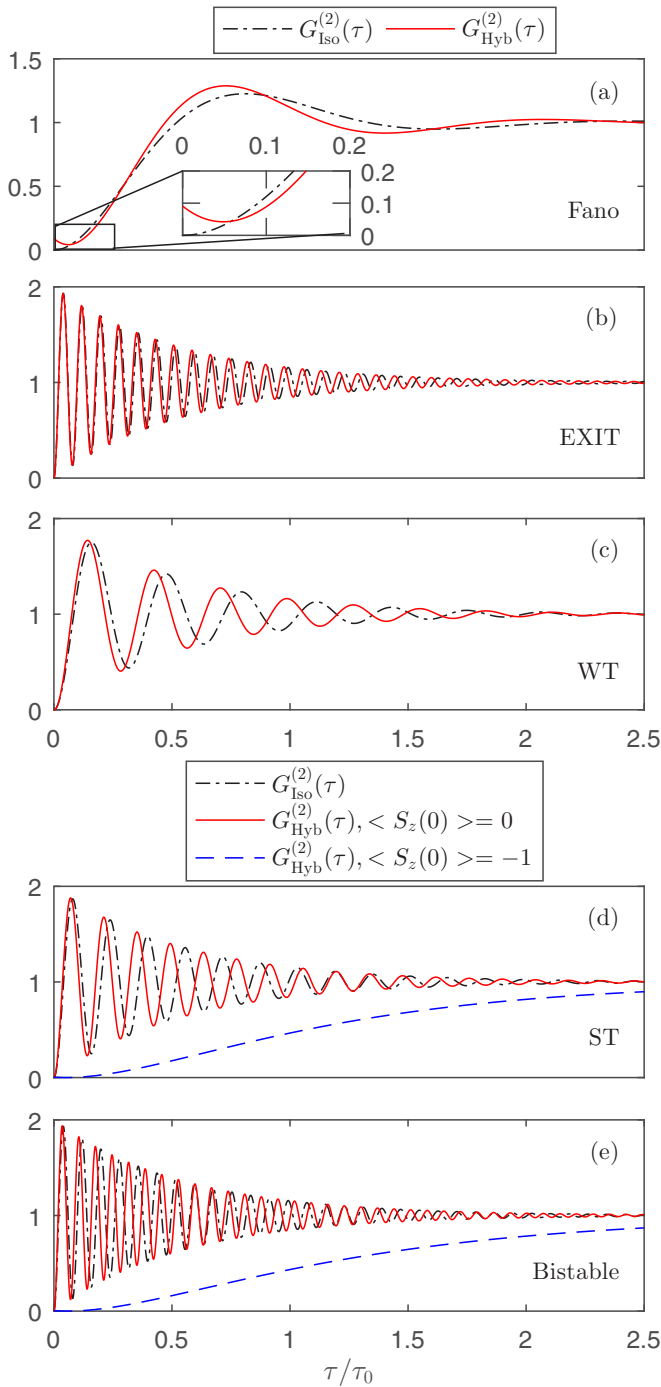FIG. 7. $G_{\mathrm{Iso}}^{(2)}(\tau)$ and $G_{\mathrm{Hyb}}^{(2)}(\tau)$ versus τ at the points (a) F_{pd}, (b) E_{pd}, (c) W_{pd}, (d) S_{pd}, and (e) B_{pd}. Here $E_{\mathrm{inc}}(t) = E_1 \cos(\omega_1 t)$, $\Delta = 0$, and $I_1 = 10^3$ W/cm^2.

FIG. 8. $G_{\mathrm{Iso}}^{(2)}(\tau)$ and $G_{\mathrm{Hyb}}^{(2)}(\tau)$ versus τ at the points (a) F_{pd}, (b) E_{pd}, (c) W_{pd}, (d) S_{pd}, and (e) B_{pd}. Here $E_{\mathrm{inc}}(t) = E_1 \cos(\omega_1 t) + E_2 \cos(\omega_2 t)$, $\omega_n \tau_0 = 48.62$, $\Delta = 0$, and $I_1 = I_2 = 250$ W/cm^2.

the magnitude but also the *phase* of the interfering fields. For example, at point S_{pd} of the phase diagram, the dipole and multipole approximations estimate $G = 193.4e^{0.64i}$ and $G = 332.5e^{0.58i}$, respectively. Consequently, the dipole approximation estimates the maximum of $\mathcal{S}_{\mathrm{Hyb}}(\omega)$ is about 3.9 times greater than that of the multipole approximation. Thus, the multipole effects manifest in the resonance fluorescence spectrum.
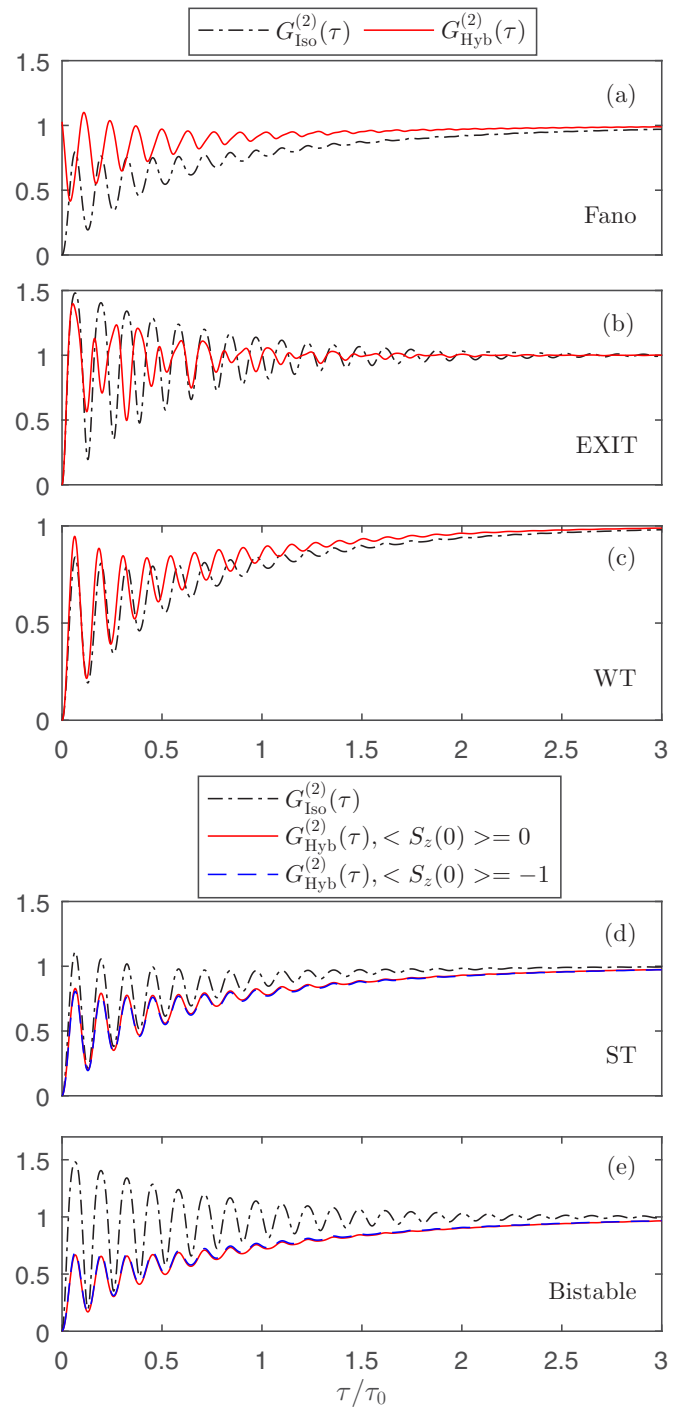
(ii) The system exhibits resonance fluorescences of different character in different regions of the phase diagram. The polarization of the incident field affects the phase diagram of the system. As an example, for $R = 13$ nm, $a = 4$ nm, and $\mu = 5\,e$ nm the system is (is not) bistable when $\boldsymbol{E}_{\mathrm{inc}} || \hat{\boldsymbol{z}}$ ($\boldsymbol{E}_{\mathrm{inc}} || \hat{\boldsymbol{x}}$) [52]. Thus, the *polarization* of the incident field can be used to control the fluorescence spectrum of the SQD-MNP system.

(iii) With recent advances in nanofabrication techniques, hybrid SQD-MNP systems are within experimental reach. For example, atomic force microscopy manipulation to position a single Au nanoparticle in the vicinity of a CdSe/ZnS quantum dot [66], strain-driven alignment of In nanocrystals on InGaAs quantum dot arrays [67,68], and ordered arrays of Au nanoparticles and PbS colloidal quantum dots [69] have been reported.

(iv) Our work can be extended in other directions. The resonance fluorescence spectrum of hybrid systems composed of multilevel SQDs, cylindrical MNPs, and many interacting SQDs and MNPs deserves attention.

In summary, the exciton-plasmon interaction is at the heart of the unique properties of the hybrid SQD-MNP system. Subjected to a monochromatic field, its absorption spectrum strongly depends on the SQD dipole moment μ and the MNP radius a. Based on this, various regions of the μ versus a phase diagram were identified [48–50,52]. Here we showed that the resonance fluorescence spectrum and the statistical properties of photons noticeably depend on both μ and a. In the strong transition and bistability regions of the phase diagram, the fluorescence spectrum and the intensity-intensity correlation function may depend on the initial state of the system. The amplitudes, frequencies, and phases of the driving fields can be invoked to tailor the fluorescence spectrum. The antibunched light and the sub-Poissonian light can be generated. Our results suggest that in view of engineering the resonance fluorescence spectrum, a hybrid SQD-MNP system is superior to an isolated SQD.

[1] B. R. Mollow, Phys. Rev. **188**, 1969 (1969).

[2] F. Y. Wu, R. E. Grove, and S. Ezekiel, Phys. Rev. Lett. **35**, 1426 (1975).

[3] G. Wrigge, I. Gerhardt, J. Hwang, G. Zumofen, and V. Sandoghdar, Nat. Phys. **4**, 60 (2008).

[4] Z. Ficek and H. S. Freedhoff, Phys. Rev. A **48**, 3092 (1993).

[5] Z. Ficek and H. S. Freedhoff, Phys. Rev. A **53**, 4275 (1996).

[6] Y. Zhu, Q. Wu, A. Lezama, D. J. Gauthier, and T. W. Mossberg, Phys. Rev. A **41**, 6574 (1990).

[7] C. C. Yu, J. R. Bochinski, T. M. V. Kordich, T. W. Mossberg, and Z. Ficek, Phys. Rev. A **56**, R4381 (1997).

[8] H. J. Carmichaelt and D. F. Walls, J. Phys. B **9**, 1199 (1976).

[9] H. J. Kimble, M. Dagenais, and L. Mandel, Phys. Rev. Lett. **39**, 691 (1977).

[10] F. Diedrich and H. Walther, Phys. Rev. Lett. **58**, 203 (1987).

[11] A. Aspect, G. Roger, S. Reynaud, J. Dalibard, and C. Cohen-Tannoudji, Phys. Rev. Lett. **45**, 617 (1980).

[12] C. A. Schrama, G. Nienhuis, H. A. Dijkerman, C. Steijsiger, and H. G. M. Heideman, Phys. Rev. A **45**, 8045 (1992).

[13] J. C. L. Carreño, E. del Valle, and F. P. Laussy, Laser Photonics Rev. **11**, 1700090 (2017).

[14] P. Michler (ed.), *Quantum Dots for Quantum Information Technologies* (Springer, Berlin, Heidelberg, 2017).

[15] I. Aharonovich, D. Englund, and M. Toth, Nat. Photonics **10**, 631 (2016).

[16] P. Senellart, G. Solomon, and A. White, Nat. Nanotechnol. **12**, 1026 (2017).

[17] P. Michler, A. Kiraz, C. Becher, W. V. Schoenfeld, P. M. Petroff, L. Zhang, E. Hu, and A. Imamoğlu, Science **290**, 2282 (2000).

[18] R. M. Stevenson, R. J. Young, P. Atkinson, K. Cooper, D. A. Ritchie, and A. J. Shields, Nature (London) **439**, 179 (2006).

[19] N. Akopian, N. H. Lindner, E. Poem, Y. Berlatzky, J. Avron, D. Gershoni, B. D. Gerardot, and P. M. Petroff, Phys. Rev. Lett. **96**, 130501 (2006).

[20] A. N. Vamivakas, Y. Zhao, C. Y. Lu, and M. Atatüre, Nat. Phys. **5**, 198 (2009).

[21] A. Ulhaq, S. Weiler, S. M. Ulrich, R. Roßbach, M. Jetter, and P. Michler, Nat. Photonics **6**, 238 (2012).

[22] X. Xu, B. Sun, P. R. Berman, D. G. Steel, A. S. Bracker, D. Gammon, and L. J. Sham, Science **317**, 929 (2007).

[23] M. Peiris, K. Konthasinghe, Y. Yu, Z. C. Niu, and A. Muller, Phys. Rev. B **89**, 155305 (2014).

[24] Y. He, Y.-M. He, J. Liu, Y.-J. Wei, H. Y. Ramírez, M. Atatüre, C. Schneider, M. Kamp, S. Höfling, C.-Y. Lu, and J.-W. Pan, Phys. Rev. Lett. **114**, 097402 (2015).

[25] S. G. Carter, V. Birkedal, C. S. Wang, L. A. Coldren, A. V. Maslov, D. S. Citrin, and M. S. Sherwin, Science **310**, 651 (2005).

[26] B. R. Mollow, Phys. Rev. A **5**, 2217 (1972).

[27] J. Zakrzewski, M. Lewenstein, and T. W. Mossberg, Phys. Rev. A **44**, 7717 (1991).

[28] S. V. Gaponenko, *Introduction to Nanophotonics* (Cambridge University Press, Cambridge, 2010).

[29] M. Achermann, J. Phys. Chem. Lett. **1**, 2837 (2010).

[30] J. Li and J. Z. Zhang, Coord. Chem. Rev. **253**, 3015 (2009).

[31] A. V. Malyshev and V. A. Malyshev, Phys. Rev. B **84**, 035314 (2011).

[32] B. S. Nugroho, V. A. Malyshev, and J. Knoester, Phys. Rev. B **92**, 165432 (2015).

[33] B. S. Nugroho, A. A. Iskandar, V. A. Malyshev, and J. Knoester, J. Chem. Phys. **139**, 014303 (2013).

[34] E. Paspalakis, S. Evangelou, S. G. Kosionis, and A. F. Terzis, J. Appl. Phys. **115**, 083106 (2014).

[35] S. M. Sadeghi, Nanotechnology **21**, 455401 (2010).

[36] D. Zhao, Y. Gu, J. Wu, J. Zhang, T. Zhang, B. D. Gerardot, and Q. Gong, Phys. Rev. B **89**, 245433 (2014).

[37] M. A. Antón, F. Carreño, S. Melle, O. G. Calderón, E. Cabrera-Granado, J. Cox, and M. R. Singh, Phys. Rev. B **86**, 155305 (2012).

[38] E. Paspalakis, S. Evangelou, and A. F. Terzis, Phys. Rev. B **87**, 235302 (2013).

[39] H. Zhang and A. O. Govorov, Phys. Rev. B **87**, 075410 (2013).

[40] E. Paspalakis, S. Evangelou, V. Yannopapas, and A. F. Terzis, Phys. Rev. A **88**, 053832 (2013).

[41] M. Otten, R. A. Shah, N. F. Scherer, M. Min, M. Pelton, and S. K. Gray, Phys. Rev. B **92**, 125432 (2015).

[42] J. D. Cox, M. R. Singh, C. von Bilderling, and A. V. Bragas, Adv. Opt. Mater. **1**, 460 (2013).

[43] M. R. Singh, Nanotechnology **24**, 125701 (2013).

[44] D. Schindel and M. R. Singh, J. Phys.: Condens. Matter **27**, 345301 (2015).

[45] M. R. Singh, M. Chandra Sekhar, S. Balakrishnan, and S. Masood, J. Appl. Phys. **122**, 034306 (2017).

[46] M. R. Singh, J. Guo, J. M. J. Cid, and J. E. De Hoyos Martinez, J. Appl. Phys. **121**, 094303 (2017).

[47] M. R. Singh and K. Black, J. Phys. Chem. C **122**, 26584 (2018).

[48] W. Zhang, A. O. Govorov, and G. W. Bryant, Phys. Rev. Lett. **97**, 146804 (2006).

[49] R. D. Artuso and G. W. Bryant, Nano Lett. **8**, 2106 (2008).

[50] R. D. Artuso and G. W. Bryant, Phys. Rev. B **82**, 195419 (2010).

[51] J. Y. Yan, W. Zhang, S. Duan, X. G. Zhao, and A. O. Govorov, Phys. Rev. B **77**, 165301 (2008).

[52] A. Mohammadzadeh and M. Miri, J. Appl. Phys. **123**, 043111 (2018).

[53] A. Ridolfo, O. Di Stefano, N. Fina, R. Saija, and S. Savasta, Phys. Rev. Lett. **105**, 263601 (2010).

[54] Y. V. Vladimirova, V. V. Klimov, V. M. Pastukhov, and V. N. Zadkov, Phys. Rev. A **85**, 053408 (2012).

[55] F. Carreño, M. A. Antón, and F. Arrieta-Yáñez, Phys. Rev. B **88**, 195303 (2013).

[56] E. S. Andrianov, A. A. Pukhov, A. P. Vinogradov, A. V. Dorofeenko, and A. A. Lisyansky, JETP Lett. **97**, 452 (2013).

[57] R.-C. Ge, C. Van Vlack, P. Yao, J. F. Young, and S. Hughes, Phys. Rev. B **87**, 205425 (2013).

[58] M. A. Antón, F. Carreño, O. G. Calderón, S. Melle, and E. Cabrera, J. Opt. **18**, 025001 (2016).

[59] F. Carreño, M. A. Antón, V. Yannopapas, and E. Paspalakis, Phys. Rev. A **94**, 013834 (2016).

[60] F. Carreño, M. A. Antón, V. Yannopapas, and E. Paspalakis, Phys. Rev. A **95**, 043825 (2017).

[61] K. E. Dorfman, F. Schlawin, and S. Mukamel, Rev. Mod. Phys. **88**, 045008 (2016).

[62] J. C. López Carreño, C. Sánchez Muñoz, D. Sanvitto, E. del Valle, and F. P. Laussy, Phys. Rev. Lett. **115**, 196402 (2015).

[63] M. O. Scully and M. S. Zubairy, *Quantum Optics* (Cambridge University Press, Cambrdige, 1997).

[64] K. Konthasinghe, M. Peiris, and A. Muller, Phys. Rev. A **90**, 023810 (2014).

[65] P. B. Johnson and R. W. Christy, Phys. Rev. B **6**, 4370 (1972).

[66] D. Ratchford, F. Shafiei, S. Kim, S. K. Gray, and X. Li, Nano Lett. **11**, 1049 (2011).

[67] A. Urbańczyk, G. J. Hamhuis, and R. Nötzel, Appl. Phys. Lett. **96**, 113101 (2010).

[68] A. Urbańczyk, G. J. Hamhuis, and R. Nötzel, Appl. Phys. Lett. **97**, 043105 (2010).

[69] M. J. Mendes, E. Hernández, E. López, P. García-Linares, I. Ramiro, I. Artacho, E. Antolín, I. Tobías, A. Martí, and A. Luque, Nanotechnology **24**, 345402 (2013).